PHYSICS

Highly selective and high-performance osmotic power generators in subnanochannel membranes enabled by metal-organic frameworks

Yi-Cheng Liu[1]*, Li-Hsien Yeh[2]*†, Min-Jie Zheng[2], Kevin C.-W. Wu[1]†

The electric organs of electric eels are able to convert ionic gradients into high-efficiency electricity because their electrocytes contain numerous "subnanoscale" protein ion channels that can achieve highly selective and ultrafast ion transport. Despite increasing awareness of blue energy production through nanochannel membranes, achieving high-performance energy output remains considerably unexplored. Here, we report on a heterogeneous subnanochannel membrane, consisting of a continuous UiO-66-NH_2 metal-organic framework (MOF) and a highly ordered alumina nanochannel membrane. In the positively charged membrane, the angstrom-scale windows function as ionic filters for screening anions with different hydrated sizes. Driven by osmosis, the subnanochannel membrane can produce an exceptionally high Br^-/NO_3^- selectivity of ~1240, hence yielding an unprecedented power of up to 26.8 W/m^2 under a 100-fold KBr gradient. Achieving ultrahigh selective and ultrafast osmotic transport in ion channel–mimetic MOF-based membranes opens previously unexplored avenues toward advanced separation technologies and energy-harvesting devices.

INTRODUCTION

Ionic gradients are in ubiquitous existence in biological membranes, and thus, selective osmotic transport of ions in biological ion channels is of fundamental significance in physiological functions of natural systems (*1*). For example, *Electrophorus electricus* (or the commonly known electric eel) is capable of converting ionic gradients into high-voltage electricity of up to 600 V using a large number of asymmetric "subnanoscale" protein ion channels on the electrocytes (Fig. 1), which can regulate fast ion transport with high selectivity (*2*). Motivated by this high-efficiency ionic gradient power system, considerable efforts have been made on the exploration of the reverse electrodialysis–based ion-selective membranes using nanoscale single-pore (*3*–*7*) and multi-pore (*8*–*12*) devices. Moreover, nanofluidics-based heterogeneous membranes (*13*–*19*), which can rectify ion transport for boosting energy harvesting from ionic gradients, have been widely exploited. However, unlike for nanopore- and nanochannel-based membranes, osmotic power harvesting with subnanochannel membranes remains significantly unexplored. Although there have been few reports on osmotic harvesting for about 1-nm-scale membranes with lamellar two-dimensional materials (*20*, *21*), the output performance was still limited due to nonuniform channel structures and limited mass transportation area, which can increase the membrane resistance for osmotic ion transport.

Metal-organic frameworks (MOFs), porous crystalline materials composed of metal clusters and organic linkers, have emerged as a promising platform for diverse applications from energy to environment (*22*–*24*) because of their narrow distribution of ordered channels, high surface area for transport, and tailorable surface properties. Although few publications have examined the potential use of the MOF-based membranes as an osmotic power generator (*25*, *26*), the output performance is still not too high (<3 W/m^2) compared with the conventional nanochannel membranes.

Most recently, a series of studies appeared, which showed that the voltage-driven ion transport can be regulated by in situ growing the UiO-66–based MOFs into a single 12-μm polyethylene terephthalate (PET) nanochannel (*27*, *28*). Significantly improved cation selectivity can be observed by tailoring surface chemistry of UiO-66 crystals. In light of their high stability in water (*29*) and numerous ordered three-dimensional channels comprising ~5- to 7-Å windows and ~8- to 11-Å cavities (fig. S1) (*30*), whose sizes are comparable to most of the hydrated ions (e.g., K^+: 6.62 Å and Cl^-: 6.64 Å) in water (*31*), the UiO-66–based MOFs are excellent candidates as an ion-selective membrane material for osmotic power harvesting. However, to the best of our knowledge, high-efficiency subnanochannel UiO-66–based MOF membranes for harvesting energy from ionic gradients are yet to be exploited.

Inspired by subnanoscale ion channels in biologic membranes, we design a heterogeneous subnanochannel membrane, UiO-66-NH_2@ANM, prepared with a continuous subnanoscale UiO-66-NH_2 MOF membrane and a highly ordered alumina nanochannel membrane (ANM) support, for osmotic energy harvesting (Fig. 1). In this ion channel–mimetic membrane, the narrow NH_2-containing window-cavity channel structures are considered as ionic filters and ionic conductors for boosting osmotic ion transport with high anion selectivity. In view of a large number of subnanochannels in UiO-66-NH_2 membrane, numerous nano/subnanochannel interfaces are formed between the two membranes of UiO-66-NH_2@ANM, and thus, the large-sized ANM can act as an ion-storage layer for improved ion transport (*17*). The resulting UiO-66-NH_2@ANM can achieve an unprecedented power density of up to 26.8 W/m^2 under a 100-fold KBr gradient, while nearly negligible power for KNO_3 at the same concentration gradient, yielding an amazingly high Br^-/NO_3^- selectivity of ~1240. Achieving ultrahigh selective and ultrafast osmotic transport in the ion channel–mimetic MOF-based membrane paves avenues for next-generation sustainable energy generation and desalination.

[1]Department of Chemical Engineering, National Taiwan University, Taipei 10617, Taiwan. [2]Department of Chemical Engineering, National Taiwan University of Science and Technology, Taipei 10607, Taiwan.
*These authors contributed equally to this work.
†Corresponding author. Email: lhyeh@mail.ntust.edu.tw (L.-H.Y.); kevinwu@ntu.edu.tw (K.C.-W.W.)

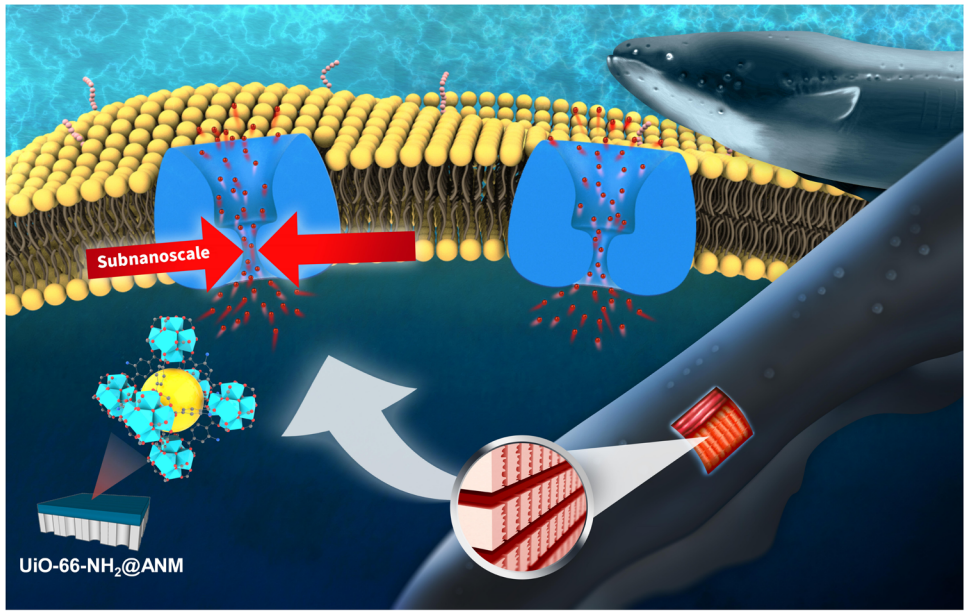

Fig. 1. Schematic depiction of the electric eel–inspired heterogeneous membrane, UiO-66-NH_2@ANM, with subnanoscale channels. The electric organ of electric eels has densely packed array of highly ion selective cell membranes known as electrocytes. An ionic concentration difference between the cell membranes can be converted into electricity by controlling the ionic fluxes with numerous asymmetric subnanoscale protein ion channels. Inspired by this, the continuous and pinhole-free UiO-66-NH_2 membrane with numerous ordered subnanochannels was fabricated onto the alumina nanochannel membrane (ANM) support, named as UiO-66-NH_2@ANM.

RESULTS

Fabrication of UiO-66-NH_2@ANM

The heterogeneous subnanochannel membrane, UiO-66-NH_2@ANM, was fabricated by in situ solvothermal synthesis of a dense UiO-66-NH_2 crystal layer on the NH_2-functionalized ANM support with the presence of an optimized amount of modulator, benzoic acid, which can assist control of the crystal size of UiO-66-NH_2 (Fig. 2A, see more details in Materials and Methods) (*32*). The ANM was fabricated by the two-step anodization strategy as reported previously (*8*), followed by postmodification with 3-aminopropyltriethoxysilane (APTES) under nitrogen to obtain the NH_2-functionalized ANM support. The modification of an APTES monolayer, which can act as a covalent linker between UiO-66-NH_2 and ANM, is important here to fabricate a continuous dense UiO-66-NH_2 crystal layer because of the poor heterogeneous nucleation between UiO-66-NH_2 and porous substrates (*33*). The successful modification of APTES onto ANM was confirmed by the x-ray photoelectron spectroscopy spectra (fig. S2A). Zeta potential measurements of the ANM and NH_2-functionalized ANM also confirmed that the latter was still positively charged in neutral solution after the modification of amine motilities on the channel walls (fig. S2B).

The successful growth of a large-scale (over 250 μm × 250 μm) continuous and pinhole-free UiO-66-NH_2 layer on the highly ordered ANM was confirmed by the top view and cross-sectional view scanning electron microscopy (SEM) images of UiO-66-NH_2@ANM (Fig. 2, B and C). The thicknesses of the UiO-66-NH_2 layer and ANM were ~750 nm and ~17.4 μm, respectively (Fig. 2C and fig. S2C), and the average pore diameter and pore density of the ANM layer were ~56 nm and ~5.2×10^9 pores/cm^2, respectively (fig. S2, D and E). The x-ray diffraction (XRD) patterns of UiO-66-NH_2@ANM also confirmed the successful synthesis of UiO-66-NH_2 crystals (fig. S2F). The contact angle measurements of UiO-66-NH_2@ANM displayed that its ANM side was hydrophilic and the UiO-66-NH_2 side was more hydrophilic (Fig. 2D), advantageous to ion and water transport. The N_2 sorption isotherms of UiO-66-NH_2 crystals revealed that they had high Brunauer-Emmett-Teller (BET) surface areas of 1106 m^2/g (fig. S3A) and were composed of ca. 6- to 7-Å window apertures and majorly about 1.24-nm cavities of ordered MOF channels (Fig. 2E). Originating from the existence of NH_2 functional groups, UiO-66-NH_2 was positively charged with a zeta potential of about 35 mV in neutral salt solution (fig. S3B), indicating an anion selectivity. The zeta potential of 35 mV at 10 mM KCl corresponds to a surface charge density of ~8.6 mC/m^2, calculated by $\sigma_s = \frac{2\varepsilon_f \kappa RT}{F}\sinh\left(\frac{F\zeta}{2RT}\right)$ (*34*), where ε_f is the dielectric constant of fluid, κ is the reciprocal of the Debye length, R is the gas constant, T is the fluid temperature, F is the Faraday constant, and ζ is the measured zeta potential of UiO-66-NH_2. The anion-selective property of the UiO-66-NH_2 layer was also confirmed by the energy-dispersive x-ray spectroscopy mappings of UiO-66-NH_2@ANM after it was immersed in 0.1 M KCl solution for 30 min (fig. S4). The strength of chlorine signals was stronger than that of potassium on the UiO-66-NH_2 surface. Because the ANM is also positively charged in neutral solution, the fabricated UiO-66-NH_2@ANM is entirely anion selective and of symmetric charge nature.

Surface charge–governed ion transport of UiO-66-NH_2@ANM

Because the UiO-66-NH_2 MOF channels fabricated comprise two major characteristic pore sizes, one of which is from triangular windows in the range of about 6 to 7 Å and the other is from octahedral cavities of diameters about 12.4 Å (Figs. 2E and 3A), the heterogeneous UiO-66-NH_2@ANM should display apparent surface charge–governed ion transport (*35*) at high electrolyte concentration. To demonstrate this, the ion transport properties of UiO-66-NH_2@ANM were examined by monitoring the transmembrane ionic current by using a custom-made electrochemical cell (see details in Materials and Methods). Figure 3B shows the current-time (*I-t*)

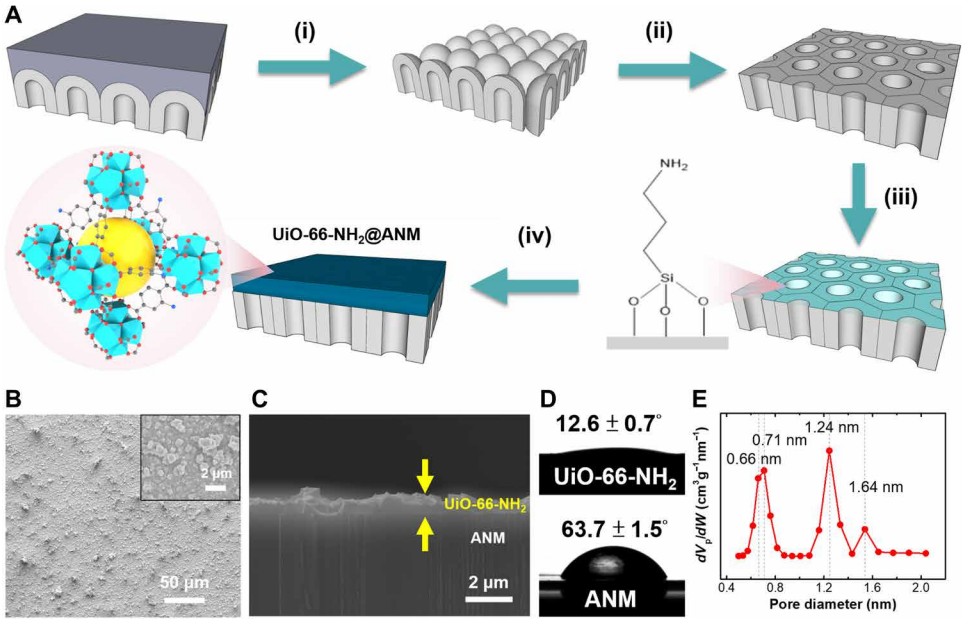

Fig. 2. Preparation and characterization of UiO-66-NH_2@ANM. (**A**) Schematic of the fabrication process of UiO-66-NH_2@ANM. (i) The residual aluminum layer on the anodized ANM was removed with $CuCl_2$ and HCl mixed solution. (ii) The barrier layer of ANM was etched by 5 wt % H_3PO_4. (iii) NH_2-functionalized ANM was obtained by surface modification of 3-aminopropyltriethoxysilane (APTES). (iv) The continuous UiO-66-NH_2 membrane was grown onto ANM by solvothermal reaction. (**B**) Top view and (**C**) cross-sectional view SEM images of UiO-66-NH_2@AMM fabricated, indicating that a continuous and pinhole-free UiO-66-NH_2 layer with thickness of ~750 nm was densely grown on the top of the ANM support. Inset in (B) represents the amplified SEM image. (**D**) Contact angle measurements of the UiO-66-NH_2 and ANM sides of the membrane. (**E**) Nominal pore size distributions of UiO-66-NH_2 calculated based on the N_2 adsorption/desorption isotherms by using the nonlocal density functional theory model.

measurement of UiO-66-NH_2@ANM recorded in 0.01 M KCl (pH 6.1) solution by alternating an applied voltage bias between +1 and −1 V. Each cycle lasted for 6 min without break, and the entire experiment was done for a total period of 48 min, displaying a superior ion transport stability of the membrane. Figure S5 further shows the current-voltage (*I*-*V*) characteristics of UiO-66-NH_2@ANM at concentrations between 0.001 and 0.1 M. For all concentrations tested, the current at the positive voltage is slightly larger than that at the negative voltage of the same magnitude, indicating that UiO-66-NH_2@ANM can rectify ionic current with the rectification ratios of about 2.06, 1.41, and 1.14 at 0.001, 0.01, and 0.1 M KCl, respectively. Similar to earlier reports with nanoscale membranes (*36*, *37*), the rectification ability of the subnanoscale UiO-66-NH_2@ANM decreases with increasing salt concentration, which can be ascribed to the stronger screened effect on surface charges of channels at higher concentration (*37*). The weak ion rectification can be attributed to the asymmetric wettabilities and pore sizes of the heterogeneous membrane prepared, both of which induce two different and opposite preferred ion transportation directions (*38*). We then further analyzed the transmembrane conductance as a function of the KCl concentration ranging from 1 μM to 3 M (Fig. 3C). As shown, the ionic conductance starts to deviate from the bulk value tendency (gray curve) when the salt concentration is below 1 M, indicating the apparent surface charge–governed ion transport phenomenon. The inset in Fig. 3C schematically depicts the Debye length of ~0.3 nm on the charged MOF channel at 1 M KCl, which is comparable to the half window size of UiO-66-NH_2 that we prepared, indicating again its subnanoscale structures. This originates from the earlier report that the channel conductance is governed by its surface charges when the overlapping of the electric double layers in the solid-state channel becomes notable (*35*). The hydrophilicity, subnanoscale pore structures, and rectified ion transport of the heterogeneous membrane prepared could shed light on the further application in osmotic power generation.

Osmotic power conversion through UiO-66-NH_2@ANM

The osmotic power conversion efficiency of UiO-66-NH_2@ANM prepared was tested with the same electrochemical cell in the presence of a salinity gradient (Fig. 4A, see details in Materials and Methods). Because both UiO-66-NH_2 and ANM are positively charged in neutral solutions, applying a salinity gradient through the composite membrane will lead to a net flow of anions, generating a diffusion potential (V_{diff}) and diffusion current (I_{diff}). Figure 4B illustrates the *I*-*V* curves of UiO-66-NH_2@ANM under the two opposite configurations of 1000-fold KCl gradient. Note that in Fig. 4B, the electrode calibration with the redox potential (V_{redox}) arising from the uneven potential drop occurring on the two Ag/AgCl electrode–solution interfaces immersed in different salinity solutions has been performed (see section S2 and table S1) (*13*). Consequently, V_{diff} and I_{diff} originating from the pure osmotic transport can be directly read from the intercepts on the voltage and current axes, respectively. Figure 4B indicates that when the concentrated solution was in contact with the UiO-66-NH_2 side, the absolute values of V_{diff} and I_{diff} were ~72.7 mV and ~1.81 μA, respectively. Under the reverse salinity gradient with the concentrated solution in contact with the ANM side, both the absolute values of V_{diff} and I_{diff} decreased to ~46.1 mV and ~1.05 μA, respectively. The preferential direction for anion transport decreases the internal resistance of the heterogeneous membrane, calculated as $R_m = V_{diff}/I_{diff}$, by approximately 9.3% in the former setup, beneficial to harvesting energy

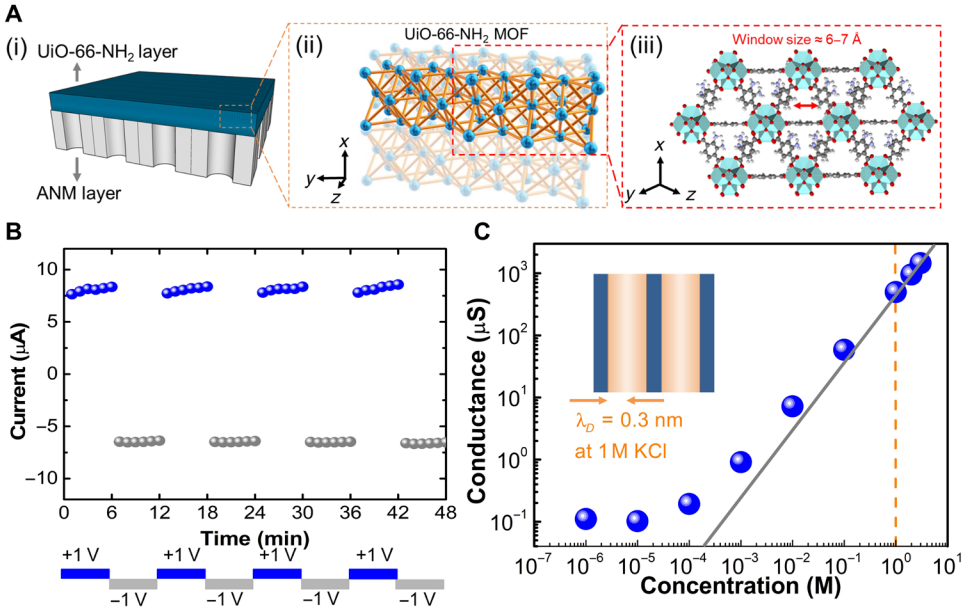

Fig. 3. Surface charge–governed ion transport in UiO-66-NH_2@ANM. (**A**) Schematic of the (i) heterogeneous UiO-66-NH_2@ANM. (ii) Illustrated lattice structure of the UiO-66-NH_2 membrane, which has (iii) ordered window size of 6 to 7 Å. (**B**) Dynamic current measurements of UiO-66-NH_2@ANM recorded in 0.01 M KCl solution with an external bias alternating between +1 and −1 V. (**C**) Transmembrane ionic conductance of UiO-66-NH_2@ANM as a function of the KCl concentration varying from 10^{-6} to 3 M. It indicates that the membrane conductance starts to deviate from the bulk value (gray line) at a high concentration of 1 M (corresponding to a Debye length of ~0.3 nm; inset), showing the apparent surface charge–governed ion transport phenomenon even in high saline condition owing to the subnanoscale channels of UiO-66-NH_2.

from salinity gradients with higher performance (*13*). Hereafter, we hence kept the compartment facing the UiO-66-NH_2 side filled with concentrated solutions in the following tests, which is consistent with earlier reports with anion selectivity of heterogeneous membranes (*14*).

As the next step, we tested the osmotic power conversion (including V_{diff} and the diffusion current density, J_{diff}) of UiO-66-NH_2@ANM under a series of concentration gradients using KCl. The lower concentration was fixed at 1 mM, and the higher concentration was elevated from 10 to 3000 mM. As shown in Fig. 4C, both the values of V_{diff} and J_{diff} generally increase with the increase of a concentration gradient. Moreover, the estimated transference numbers of anions (t^-) for the concentration gradient varying from 10- to 3000-fold are all higher than 0.5 (table S1), indicating the anion selectivity (*14*) of the heterogeneous membrane prepared. With increasing KCl gradient, the maximum energy conversion efficiency (η_{max}) decreases sharply from 33.0 to 8.93% (table S1), similar to the earlier reports with solid nanopore membranes (*13*, *14*).

The practical harvested osmotic power can be estimated by transferring it to an external circuit with an electric load (R_L). We then investigated the output current density and power density of UiO-66-NH_2@ANM as a function of the external load resistance under a series of the concentration gradients from 5- to 500-fold (Fig. 4D). Here, the power generated can be calculated as $P = I^2 \times R_L$, where I is the measured current. The current density decreases with increasing resistance, and hence, the power density will go through a local maximum value at conditions at which the external resistance is equal to the internal resistance of the membrane (*13*). As shown in Fig. 4D, the maximum output power densities were about 2.19, 4.93, and 7.12 W/m^2 under the 5-, 50-, and 500-fold KCl gradients, respectively. At the 50-fold salinity gradient at which the seawater is mixed with river water, the power density achieved is impressive and comparable to most of the previously reported heterogeneous membranes (*13*–*19*), but the output is still below the value of the commercial benchmark (5 W/m^2).

We also tested the osmotic power generation of UiO-66-NH_2@ANM by mixing artificial seawater (500 mM NaCl) and river water (10 mM NaCl). As shown in fig. S6, the maximum output power density was about 2.96 W/m^2 under this 50-fold NaCl concentration gradient. Note that although the achieved power density is smaller than the above value with using KCl (4.93 W/m^2) under the same concentration gradient, it is still higher than all the reported state-of-the-art anion-selective nanochannel membranes (*14*, *15*, *39*–*41*) to the best of our knowledge (table S2). The demoted osmotic power when using NaCl can be attributed to the larger hydrated diameter of Na^+ ions (7.16 Å) than the K^+ ions (6.62 Å) (*31*). However, because the subnanoscale membrane is highly anion selective and composed of a large number of ordered window-cavity channel structures, the demotion in osmotic power with other larger-size cations is not notable.

Highly selective and high-performance osmotic power generation

Note that the hydrated diameter of the major transporting anions, Cl^-, considered here is 6.64 Å (*31*), which is within the window sizes (ca. 6 to 7 Å) of UiO-66-NH_2 that we prepared. This drives us to think whether there is a possibility to use the other electrolytes (e.g., KBr) with a smaller hydrated anion diameter for improved osmotic power generation. We then investigated the osmotic power generation of the heterogeneous subnanochannel membrane, UiO-66-NH_2@ANM, by using four anion types of electrolytes with different hydrated diameters (Fig. 5). Here, we fixed the higher concentration at a high saline condition of 1000 mM (corresponding to a Debye length of 0.3 nm) to minimize the surface charge effect and the lower

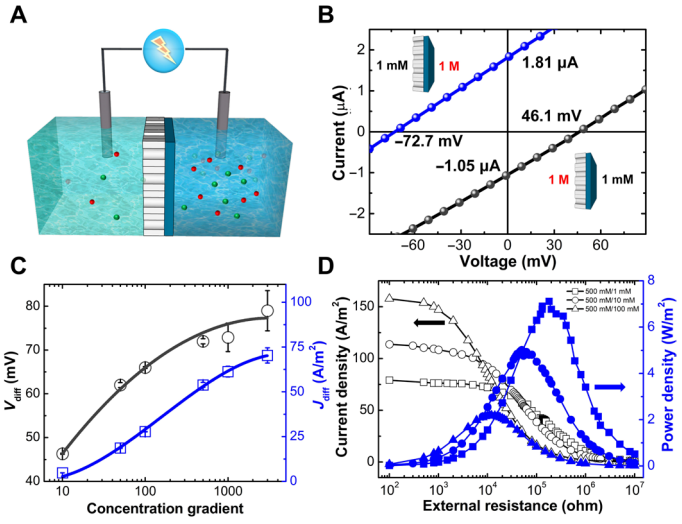

Fig. 4. Osmotic energy conversion of UiO-66-NH_2@ANM. (**A**) Schematic of our osmotic energy-harvesting device under a salinity gradient. (**B**) *I-V* curves of UiO-66-NH_2@ANM recorded under two opposite configurations of 1000-fold KCl gradient, where the redox potential contribution has been subtracted. The internal resistance (R_m) decreases by ~9.3% when the UiO-66-NH_2 layer faced a concentrated solution. (**C**) Diffusion potential (V_{diff}) and diffusion current (I_{diff}) as a function of concentration gradient. The lower concentration in contact with the ANM side was fixed at 1 mM. (**D**) Current density (open symbols) and power density (solid symbols) harvested under various KCl concentration gradients. The maximum output power densities achieved were ~2.19, 4.93, and 7.12 W/m^2 under 5-, 50-, and 500-fold concentration gradients, respectively.

concentration at 10 mM. Because the heterogeneous subnanochannel membrane is entirely positively charged, the difference in osmotic powers shown in Fig. 5 comes primarily from major transporting anions. The current densities of UiO-66-NH_2@ANM in KBr and KCl were over one order of magnitude higher than those in KNO_3 and Na_2SO_4 (Fig. 5A). The achieved maximum power densities were ca. 26.8, 11.0, 0.0216, and 0.0497 W/m^2 for KBr, KCl, KNO_3, and Na_2SO_4, respectively (Fig. 5B). Similar to the behaviors of current density, UiO-66-NH_2@ANM outputs the osmotic power densities in KBr and KCl that are higher than those in KNO_3 and Na_2SO_4 systems. While at first unexpected, these results are supported by the recordings of osmosis-driven short-circuit currents even using the other independently prepared membrane (Fig. 5C). It is worth noting that to the best of our knowledge, the maximum power density of 26.8 W/m^2 enabled by the present subnanochannel MOF membrane in such high saline conditions outperforms all of the state-of-the-art membranes reported (table S3) (*15*, *42*–*44*), although a five times lower concentration gradient is used here. Even under such a high concentration gradient, the conversion efficiency is enhanced up to 43.7%, along with an ultrahigh transference anion number of 0.968 (table S1). Compared with the other nanochannel membranes (*13*–*19*, *42*–*44*), where the efficiencies are generally below 35% under a 50-fold salinity gradient, our heterogeneous subnanochannel membrane can harvest more energy from even a higher salinity gradient. The boosted osmotic power performance is explained by the consequent effects of (i) the hydrophilicity and numerous narrow window-cavity channels of the continuous UiO-66-NH_2 layer; (ii) the highly ordered channel structure of the ANM layer behaving as an ion-storage layer (*17*), which can greatly enrich ions stored in the nanochannels; and (iii) the ionic diode effect inducing directional ion transport for enhanced current (*18*). Of UiO-66-NH_2, the sub-1-nm-scale windows can function as ionic filters for screening hydrated anions and enhancing ion selectivity, whereas the nanometer-scale cavities can act as ionic conductors for boosting osmotic ion transport (*45*).

To quantity the magnitude by which the importance of the subnanoscale UiO-66-NH_2 layer contributes to the selective and promoted osmotic transport, we then compared the output powers from the present subnanoscale UiO-66-NH_2@ANM with those from the nanoscale ANM in different anion-type electrolytes at a 100-fold salinity gradient (Fig. 5D, fig. S7, and table S4). Note that in this study, we adopted the ~25-nm-diameter ANM in the comparison because of its apparently higher selectivity than the ~56-nm-diameter ANM. In KBr and KCl, the subnanochannel membrane UiO-66-NH_2@ANM outputted powers notably higher than the ANM; however, the reverse trends were observed in KNO_3 and Na_2SO_4. Compared with the nanoscale ANM, UiO-66-NH_2@ANM showed the appreciably amplified power densities of up to 1.92-and 1.13-fold in KBr and KCl, respectively. However, in KNO_3 and Na_2SO_4, the powers generated by UiO-66-NH_2@ANM largely decreased by 96.9 and 87.6%, respectively. Similar behavior can also be found in the osmosis-driven short-circuit currents between UiO-66-NH_2@ANM and ANM depicted in Fig. 5C and fig. S7C. Note that the achieved maximum power densities of the ANM were as low as ~0.69 and ~0.40 W/m^2 in KNO_3 and Na_2SO_4, respectively, ascribed to the strong absorption of nitrate and sulfate ions by alumina surfaces (*46*), which leads to an apparent decrease of the surface charges on the ANM. Subsequently, in the same electrolytes, the osmotic power was further decreased to approaching zero value using the heterogeneous subnanochannel membrane UiO-66-NH_2@ANM. Apparently, the promoted and demoted osmotic power efficiencies between UiO-66-NH_2@ANM and ANM stem from the existence of the subnanoscale window-cavity channel structures of the UiO-66-NH_2 membrane layer, which can function as either ionic conductors for boosting osmotic ion transport or ionic filters for hindering ion passage. Although the presence of NH_2 groups is capable of facilitating the anion transport, the angstrom-sized pore windows play a role on sieving hydrated anions.

As the next step, we analyzed the selectivity ratios of the present subnanoscale UiO-66-NH_2@ANM and those of the nanoscale ANM (Fig. 5E and table S4). Because UiO-66-NH_2@ANM outputs the lowest power in KNO_3, the selectivities of the subnanochannel and nanochannel membranes reported here were estimated as a ratio of osmotic powers recorded in different anion types of electrolytes and KNO_3, which is different from the earlier reports using the voltage-driven ionic currents/conductances to calculate ion selectivity (*45*, *47*), to emphasize the contribution of osmotic ion transport. The subnanoscale UiO-66-NH_2@ANM achieved the amazingly high Br^-/NO_3^- and Cl^-/NO_3^- selectivities of up to ~1240 and ~509, respectively, but the nanoscale ANM can enable the corresponding selectivities of ~13.3 and ~7.46 only. It is known that ions in water are hydrated and the hydrated ionic diameters are larger than the dehydrated ones (table S5) (*31*). The sequence of the four major transporting anions considered is Br^- (6.62 Å) < Cl^- (6.64 Å) < NO_3^- (6.70 Å) < SO_4^{2-} (7.58 Å). In the ANM, whose pore diameter is apparently larger than the diameter of hydrated ions, all transporting ions can pass through the nanoscale channels (fig. S7D). Therefore, the osmotic power performance and selectivity of the positively charged ANM depend on the adsorption affinity of anions to the

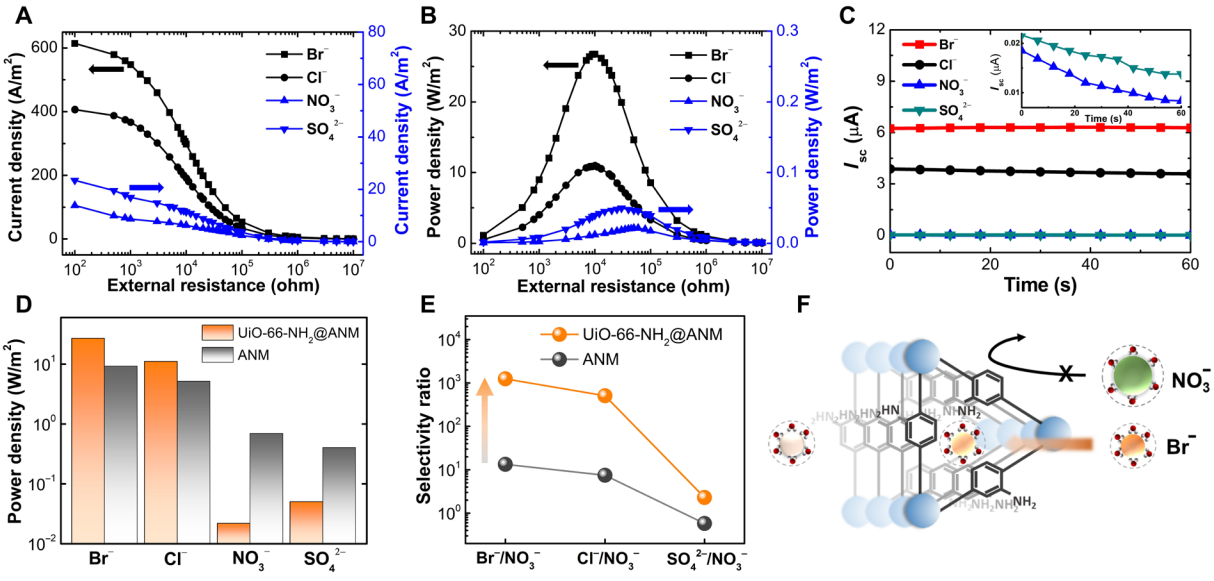

Fig. 5. Highly selective and high-performance osmotic power of UiO-66-NH_2@ANM. The effect of anion salt types on the (**A**) current density, (**B**) power density, and (**C**) short-circuit current (I_{sc}) of UiO-66-NH_2@ANM generated in 1000 mM/10 mM concentration gradient. The maximum power densities with Br^-, Cl^-, NO_3^-, and SO_4^{2-} were ~26.8, 11.0, 0.0216, and 0.0497 W/m^2, respectively. (**D**) Comparison of the output osmotic powers between the subnanoscale UiO-66-NH_2@ANM and the nanoscale ANM (with pore diameter of 25 nm) in different types of salts. (**E**) The selectivity ratios of the subnanoscale UiO-66-NH_2@ANM and the nanoscale ANM were calculated on the basis of their output powers in various salt systems shown in (D). UiO-66-NH_2@ANM can exhibit an unprecedented Br^-/ NO_3^- selectivity of ~1240. (**F**) Schematic depiction of the anion-selective property of subnanoscale UiO-66-NH_2@ANM based on the size exclusion effect.

alumina channels and ionic diffusivities. However, the subnanoscale UiO-66-NH_2 channels that we prepared contain window apertures with the size of about 6 to 7 Å. If the hydrated anions (e.g., NO_3^- and SO_4^{2-}) have a size larger than the critical screening size of UiO-66-NH_2 subnanochannels, a large number of anions will be blocked (Fig. 5F), leading to an extremely low osmotic power performance. On the contrary, the hydrated anions with smaller sizes (e.g., Br^- and Cl^-) are able to pass through the UiO-66-NH_2 subnanochannels, thus yielding an ultrahigh selectivity and performance osmotic power harvesting in UiO-66-NH_2@ANM, attributed to the combined effects of numerous hydrophilic window-cavity channels and nano/subnanochannel interfaces functioned as an ion-storage layer (*17*). It is also worth noting that the osmotic power performance and selectivity of UiO-66-NH_2@ANM do not depend on the mobilities of anions. For example, the mobility of Cl^- is faster than that of Br^- (table S5), but the short-circuit current and output power density achieved with the latter are apparently larger than those with the former.

We also tested the effects of pH and testing area on the osmotic power generation of UiO-66-NH_2@ANM in 1000 mM/10 mM KBr gradient (figs. S8 and S9). As shown in fig. S8, the output power decreases with the increase of pH and drops apparently when pH increases from pH 6 to 9, which can be ascribed to the notable decrease in surface charges of UiO-66-NH_2 at pH 9 (fig. S3B) due to the presence of more uncharged, deprotonated NH_2 functional groups. The output power also decreases with the increase of testing membrane area (fig. S9), which is expected because the enhanced access resistance and reduced ion selectivity (*18*) will undermine the conversion performance. However, we have to emphasize that our heterogeneous subnanochannel membrane was still able to achieve high-performance power as high as ~4.4 W/m^2 when using a testing area of 0.785 mm^2 [more than 26-fold larger than the commonly used testing area of 0.03 mm^2 (*15*, *42*–*44*)]. This suggests the potential use of the UiO-66–based membranes in future industrial large-scale membrane applications.

Stability test of UiO-66-NH_2@ANM

We also tested the stability of UiO-66-NH_2@ANM in aqueous solutions. The UiO-66-NH_2 side, after immersing the heterogeneous membrane in deionized water for 1 month, still kept continuous and dense structure (Fig. 6A), along with high crystallinity (Fig. 6B). We also soaked the UiO-66-NH_2 sample in high (i.e., 0.5 M) and different saline (e.g., KCl, KBr, KNO_3, and Na_2SO_4) environments for 7 days. XRD results shown in fig. S10 indicated that the structure of UiO-66-NH_2 retains its high crystallinity. The N_2 sorption isotherms of UiO-66-NH_2 shown in fig. S11 revealed that UiO-66-NH_2 can still contain about 77 and 75% BET surface areas after being soaked in 0.5 M KCl and 0.5 M KBr solutions, respectively. The slight decrease in surface area can be ascribed to the adsorption of high-concentration anions. The BET isotherm results validate again the high structural ability of UiO-66-NH_2 in saline environments. Such a good water and chemical stability of the UiO-66 MOF has been explained to be attributed to the strong Zr—O bond and the compact structure of metal clusters (*29*). Figure 6C illustrates the recordings of the short-circuit current of UiO-66-NH_2@ANM in 500 mM/10 mM KCl. The membrane can still retain 90.8% stable current operated for continuous 12 hours, revealing the potential of long-term operation for future application.

To further demonstrate the stability of osmotic power conversion performance with UiO-66-NH_2@ANM, we independently prepared a new membrane and tested its output power density in 1000 mM/10 mM KBr gradient for seven continuous days. As shown in Fig. 6D and fig. S12, only 12.8% decrease (from 26.5 to 23.1 W/m^2) of output power density can be observed. In addition, the cross-sectional

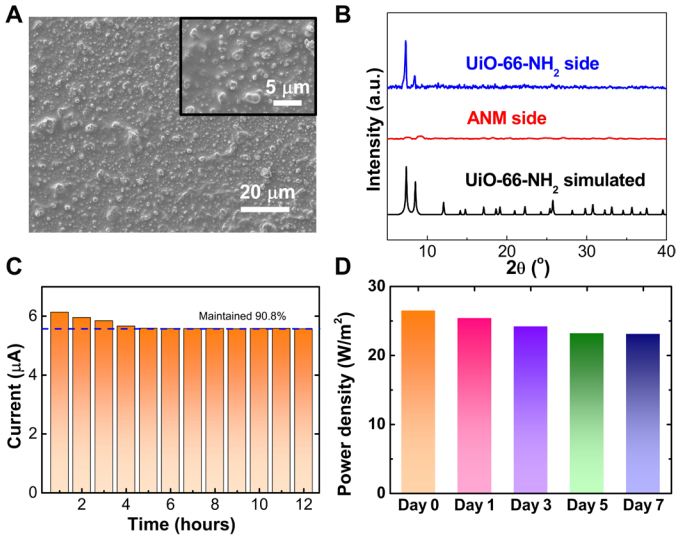

Fig. 6. Stability of UiO-66-NH_2@ANM in aqueous solution. (**A**) Top view SEM images and (**B**) XRD patterns of UiO-66-NH_2@ANM tested after being soaked in aqueous solution for 30 days at room temperature. a.u., arbitrary units. (**C**) Short-circuit current of UiO-66-NH_2@ANM recorded in 500 mM/10 mM KCl gradient for continuous 12 hours. (**D**) Output power density of UiO-66-NH_2@ANM recorded in 1000 mM/10 mM KBr gradient for continuous 1 week.

SEM image shown in fig. S13 also reveals that after being soaked in high saline conditions, the UiO-66-NH_2 membrane layer still kept its continuous and dense structure. All these results shown demonstrate the high structure and osmotic power conversion stability of our heterogeneous subnanochannel membrane, UiO-66-NH_2@ANM, in high saline environments.

DISCUSSION

In summary, we report a strategy to fabricate the novel heterogeneous membrane, consisting of a thin layer of continuous subnanochannel UiO-66-NH_2 membrane and a highly ordered ANM support, to harvest osmotic power with improved selectivity and performance. It has been shown here that the UiO-66-NH_2 layer is hydrophilic, positively charged, and composed of a large number of angstrom-scale (ca. 6 to 7 Å) windows and nanometer-scale cavities, yielding several unexpected but outstanding osmotic transport properties. The numerous subnanoscale window-cavity channel structures act as ionic filters and conductors for boosting selective osmotic transport of ions, and the introduction of the ANM functions as an ion-storage layer for improved energy harvesting. UiO-66-NH_2@ANM can generate an unprecedented power density as high as 26.8 W/m^2 together with 43.7% efficiency under a 100-fold KBr gradient, both of which are the highest values compared with the other state-of-the-art membranes (*15*, *42*–*44*). The incorporation of the dense UiO-66-NH_2 layer renders the angstrom-sized pores highly selective toward hydrated anions with different sizes. As a consequence, the heterogeneous subnanochannel membrane fabricated, UiO-66-NH_2@ANM, can achieve the ultrahigh Br^-/NO_3^- selectivity of ~1240 on the basis of a ratio of osmotic powers generated.

This proof-of-concept study demonstrates the potential use of large-scale and continuous MOF-based subnanochannel membranes for highly selective and high-performance osmotic power generators. The prototype work of anion-selective subnanochannel membrane can be further extended to cation-selective ones by tailoring functionality chemistry of UiO-66 pores, which will be identified as our future work and can lead to a new discovery of ionic devices. The mechanical property of heterogeneous subnanochannel membranes is expected to be improved by introducing high tensile strength porous polymer membranes as substrate support (*18*). We will also attempt different types of MOF membranes and identify experimental conditions, which may offer ultrafast osmotic ion transport and high-efficiency blue energy conversion in seawater-simulated (NaCl) conditions.

MATERIALS AND METHODS

Materials and chemicals

The detailed information of all materials and chemicals is summarized as follows: aluminum foil (Al, 99.9995%; Strem Chemicals), oxalic acid ($H_2C_2O_4$, 99.8%; Showa), perchloric acid ($HClO_4$, 70%; Showa), chromium oxide (CrO_3, 99%; Showa), hydrochloric acid (HCl, 37%; Sigma-Aldrich), copper chloride ($CuCl_2{\cdot}2H_2O$, 97%; Showa), phosphoric acid (H_3PO_4, 85%; Scharlau), 3-triethoxysilylpropylamine (APTES, ≥98%; Sigma-Aldrich), toluene (99.5%, JT Baker), zirconium (IV) chloride ($ZrCl_4$, 99.5+%-Zr; Strem Chemicals), *N*,*N*-dimethylformamide (DMF) (anhydrous, Macron), 2-aminoterephtalic acid (BDC-NH_2, 99%; Sigma-Aldrich), benzoic acid (≥99.5%; TCI), sodium chloride (NaCl, 99%; Sigma-Aldrich), potassium chloride (KCl, 99%; JT Baker), potassium bromide (KBr, ≥99%; Honeywell Fluka), potassium nitrate (KNO_3, 99%; Alfa Aesar), and sodium sulfate (Na_2SO_4, 99%; Macron). Other solvents were purchased from ECHO Chemical Co. Ltd., Taiwan. All chemicals were used as provided. All aqueous solutions were prepared with deionized water (18.2 megohm·cm, Milli-Q).

Preparation of NH_2-functionalized ANM support

The ANM support with highly ordered straight channels was fabricated using the two-step anodization process as reported previously (*8*). First, a high-purity Al sheet was washed with acetone, ethanol, and water in sequence and then electrochemically polished with the $HClO_4$/ethanol solution (1:4 v/v) at 20 V for 90 s. The first anodization was carried out in 0.3 M oxalic acid under 50 V at 20°C for 30 min. Then, the disordered oxide layer was removed by the mixed solution (H_3PO_4/CrO_3/water) at 60°C for 1 hour. The second anodization was performed under the same condition of first anodization for 1 hour. To obtain a free-standing ANM support, the remaining aluminum was removed by the mixed solution ($CuCl_2$/HCl/water), followed by the etching of barrier layer carried out by 5 weight % (wt %) H_3PO_4 for 55 min at 30°C. Upon completion of the above steps, the ANM was then treated with APTES (0.02 M, in 40 ml of toluene) at 50°C for 3 hours under N_2 environment. After washing the modified ANM three times with toluene and ethanol, the membrane was cured in an oven at 110°C for 1 hour to ensure modification.

Fabrication of UiO-66-NH_2@ANM

First, a mixture of $ZrCl_4$ (0.116 g, 0.5 mmol), benzoic acid (5.06 g, 41.4 mmol), and DMF (30 ml) solution was stirred for 30 min in beaker. Then, the solution was transferred to 50-ml Teflon container and heated at 80°C for 2 hours. After cooling to room temperature,

BDC-NH_2 (0.0906 g, 0.5 mmol) was added in the container and then sonicated for 30 min. Subsequently, the container was placed into a man-made stainless steel autoclave, in which the ANM support was secured vertically with a Teflon holder to ensure the in situ growth of a dense UiO-66-NH_2 layer on one side of the ANM. The autoclave was placed in an oven reacting at 120°C for 24 hours. After cooling to room temperature, the as-prepared membrane was immersed in DMF for 1 hour, followed by immersing in ethanol overnight. Last, UiO-66-NH_2@ANM can be obtained after drying at 45°C overnight.

Electrical measurement

The tested membranes were mounted between two halves of a homemade electrochemical cell (fig. S14). The ion transport properties and subsequent osmotic power conversion tests were all performed with a Keithley 6487 picoammeter (Keithley Instruments, Cleveland, Ohio). A pair of Ag/AgCl electrodes was used, and the working electrode was placed in the compartment facing the UiO-66-NH_2 side for all measurements. For the analysis of ion transport, the *I-t* result was conducted in 0.01 M KCl solution by alternating an applied voltage bias between +1 and −1 V, and each cycle lasted for 6 min without break. The *I-V* results were recorded by changing the voltage between −2 and +2 V with 0.2-V steps, and the transmembrane conductance was calculated at +1 V. For the *I-V* curves in the osmotic energy conversion analyses, the contribution of the redox potential, obtained by measuring the potential of the same testing non–ion-selective microhole silicon wafer without UiO-66-NH_2@ANM, has been deducted. For the output current density and power density measurements, an effective testing area of 0.03 mm^2 for ion transport was divided, consistent with previous studies (*15*, *42*–*44*).

SUPPLEMENTARY MATERIALS

Supplementary material for this article is available at http://advances.sciencemag.org/cgi/content/full/7/10/eabe9924/DC1

REFERENCES AND NOTES

1. B. Hille, *Ion Channels of Excitable Membranes* (Sinauer Associates, 2001).
2. J. Xu, D. A. Lavan, Designing artificial cells to harness the biological ion concentration gradient. *Nat. Nanotechnol.* **3**, 666–670 (2008).
3. W. Guo, L. X. Cao, J. C. Xia, F. Q. Nie, W. Ma, J. M. Xue, Y. L. Song, D. B. Zhu, Y. G. Wang, L. Jiang, Energy harvesting with single-ion-selective nanopores: A concentration-gradient-driven nanofluidic power source. *Adv. Funct. Mater.* **20**, 1339–1344 (2010).
4. A. Siria, P. Poncharal, A. L. Biance, R. Fulcrand, X. Blase, S. T. Purcell, L. Bocquet, Giant osmotic energy conversion measured in a single transmembrane boron nitride nanotube. *Nature* **494**, 455–458 (2013).
5. J. D. Feng, M. Graf, K. Liu, D. Ovchinnikov, D. Dumcenco, M. Heiranian, V. Nandigana, N. R. Aluru, A. Kis, A. Radenovic, Single-layer MoS2 nanopores as nanopower generators. *Nature* **536**, 197–200 (2016).
6. J. P. Hsu, T. C. Su, P. H. Peng, S. C. Hsu, M. J. Zheng, L. H. Yeh, Unraveling the anomalous surface-charge-dependent osmotic power using a single funnel-shaped nanochannel. *ACS Nano* **13**, 13374–13381 (2019).
7. C. Y. Lin, C. Combs, Y. S. Su, L. H. Yeh, Z. S. Siwy, Rectification of concentration polarization in mesopores leads to high conductance ionic diodes and high performance osmotic power. *J. Am. Chem. Soc.* **141**, 3691–3698 (2019).
8. L. H. Yeh, Z. Y. Huang, Y. C. Liu, M. J. Deng, T. H. Chou, H. C. O. Yang, T. Ahamad, S. M. Alshehri, K. C. W. Wu, A nanofluidic osmotic power generator demonstrated in polymer gel electrolytes with substantially enhanced performance. *J. Mater. Chem. A* **7**, 26791–26796 (2019).
9. T. J. Ma, E. Balanzat, J. M. Janot, S. Balme, Nanopore functionalized by highly charged hydrogels for osmotic energy harvesting. *ACS Appl. Mater. Interfaces* **11**, 12578–12585 (2019).
10. V. P. Mai, R. J. Yang, Boosting power generation from salinity gradient on high-density nanoporous membrane using thermal effect. *Appl. Energy* **274**, 115294 (2020).
11. X. Liu, M. He, D. Calvani, H. Y. Qi, K. Gupta, H. J. M. de Groot, G. J. A. Sevink, F. Buda, U. Kaiser, G. F. Schneider, Power generation by reverse electrodialysis in a single-layer nanoporous membrane made from core-rim polycyclic aromatic hydrocarbons. *Nat. Nanotechnol.* **15**, 307–312 (2020).
12. J. Hwang, T. Sekimoto, W. L. Hsu, S. Kataoka, A. Endo, H. Daiguji, Thermal dependence of nanofluidic energy conversion by reverse electrodialysis. *Nanoscale* **9**, 12068–12076 (2017).
13. J. Gao, W. Guo, D. Feng, H. T. Wang, D. Y. Zhao, L. Jiang, High-performance ionic diode membrane for salinity gradient power generation. *J. Am. Chem. Soc.* **136**, 12265–12272 (2014).
14. Z. Zhang, X. Sui, P. Li, G. H. Xie, X. Y. Kong, K. Xiao, L. C. Gao, L. P. Wen, L. Jiang, Ultrathin and ion-selective Janus membranes for high-performance osmotic energy conversion. *J. Am. Chem. Soc.* **139**, 8905–8914 (2017).
15. X. B. Zhu, J. R. Hao, B. Bao, Y. H. Zhou, H. B. Zhang, J. H. Pang, Z. H. Jiang, L. Jiang, Unique ion rectification in hypersaline environment: A high-performance and sustainable power generator system. *Sci. Adv.* **4**, eaau1665 (2018).
16. K. X. Chen, L. N. Yao, B. Su, Bionic thermoelectric response with nanochannels. *J. Am. Chem. Soc.* **141**, 8608–8615 (2019).
17. W. W. Xin, Z. Zhang, X. D. Huang, Y. H. Hu, T. Zhou, C. C. Zhu, X. Y. Kong, L. Jiang, L. P. Wen, High-performance silk-based hybrid membranes employed for osmotic energy conversion. *Nat. Commun.* **10**, 3876 (2019).
18. Z. Zhang, L. He, C. C. Zhu, Y. C. Qian, L. P. Wen, L. Jiang, Improved osmotic energy conversion in heterogeneous membrane boosted by three-dimensional hydrogel interface. *Nat. Commun.* **11**, 875 (2020).
19. J. Jung, J. Kim, H. S. Lee, I. S. Kang, K. Choi, Multi-asymmetric ion-diode membranes with superior selectivity and zero concentration polarization effect. *ACS Nano* **13**, 10761–10767 (2019).
20. S. Hong, F. W. Ming, Y. Shi, R. Y. Li, I. S. Kim, C. Y. Y. Tang, H. N. Alshareef, P. Wang, Two-dimensional Ti3C2TxMXene membranes as nanofluidic osmotic power generators. *ACS Nano* **13**, 8917–8925 (2019).
21. Z. Zhang, P. P. Zhang, S. Yang, T. Zhang, M. Loffler, H. H. Shi, M. R. Lohe, X. L. Feng, Oxidation promoted osmotic energy conversion in black phosphorus membranes. *Proc. Natl. Acad. Sci. U.S.A.* **117**, 13959–13966 (2020).
22. H. Furukawa, K. E. Cordova, M. O'Keeffe, O. M. Yaghi, The chemistry and applications of metal-organic frameworks. *Science* **341**, 1230444 (2013).
23. F. K. Shieh, S. C. Wang, C. I. Yen, C. C. Wu, S. Dutta, L. Y. Chou, J. V. Morabito, P. Hu, M. H. Hsu, K. C. W. Wu, C. K. Tsung, Imparting functionality to biocatalysts via embedding enzymes into nanoporous materials by a de novo approach: Size-selective sheltering of catalase in metal-organic framework microcrystals. *J. Am. Chem. Soc.* **137**, 4276–4279 (2015).
24. R. R. Salunkhe, Y. V. Kaneti, Y. Yamauchi, Metal-organic framework-derived nanoporous metal oxides toward supercapacitor applications: Progress and prospects. *ACS Nano* **11**, 5293–5308 (2017).
25. R. R. Li, J. Q. Jiang, Q. Q. Liu, Z. Q. Xie, J. Zhai, Hybrid nanochannel membrane based on polymer/MOF for high-performance salinity gradient power generation. *Nano Energy* **53**, 643–649 (2018).
26. C. Wang, F. F. Liu, Z. Tan, Y. M. Chen, W. C. Hu, X. H. Xia, Fabrication of bio-inspired 2D MOFs/PAA hybrid membrane for asymmetric ion transport. *Adv. Funct. Mater.* **30**, 1908804 (2019).
27. X. Y. Li, H. C. Zhang, J. Hou, R. W. Ou, Y. L. Zhu, C. Zhao, T. Y. Qian, C. D. Easton, C. Selomulya, M. R. Hill, H. T. Wang, Sulfonated sub-1-nm metal-organic framework channels with ultrahigh proton selectivity. *J. Am. Chem. Soc.* **142**, 9827–9833 (2020).
28. J. Lu, H. C. Zhang, J. Hou, X. Y. Li, X. Y. Hu, Y. X. Hu, C. D. Easton, Q. Y. Li, C. H. Sun, A. W. Thornton, M. R. Hill, X. W. Zhang, G. P. Jiang, J. Z. Liu, A. J. Hill, B. D. Freeman, L. Jiang, H. T. Wang, Efficient metal ion sieving in rectifying subnanochannels enabled by metal-organic frameworks. *Nat. Mater.* **19**, 767–774 (2020).
29. X. L. Liu, N. K. Demir, Z. T. Wu, K. Li, Highly water-stable zirconium metal organic framework UiO-66 membranes supported on alumina hollow fibers for desalination. *J. Am. Chem. Soc.* **137**, 6999–7002 (2015).
30. P. S. Barcia, D. Guimaraes, P. A. P. Mendes, J. A. C. Silva, V. Guillerm, H. Chevreau, C. Serre, A. E. Rodrigues, Reverse shape selectivity in the adsorption of hexane and xylene isomers in MOF UiO-66. *Microporous Mesoporous Mater.* **139**, 67–73 (2011).
31. E. R. Nightingale Jr., Phenomenological theory of ion solvation. Effective radii of hydrated ions. *J. Phys. Chem.* **63**, 1381–1387 (1959).
32. A. Schaate, P. Roy, A. Godt, J. Lippke, F. Waltz, M. Wiebcke, P. Behrens, Modulated synthesis of Zr-based metal-organic frameworks: From nano to single crystals. *Chem. Eur. J.* **17**, 6643–6651 (2011).
33. L. L. Wan, C. Zhou, K. Xu, B. Feng, A. S. Huang, Synthesis of highly stable UiO-66-NH2 membranes with high ions rejection for seawater desalination. *Microporous Mesoporous Mater.* **252**, 207–213 (2017).
34. L. H. Yeh, S. Xue, S. W. Joo, S. Qian, J. P. Hsu, Field effect control of surface charge property and electroosmotic flow in nanofluidics. *J. Phys. Chem. C* **116**, 4209–4216 (2012).
35. Y. Ma, L. H. Yeh, C. Y. Lin, L. J. Mei, S. Z. Qian, pH-regulated ionic conductance in a nanochannel with overlapped electric double layers. *Anal. Chem.* **87**, 4508–4514 (2015).

36. Q. Q. Zhang, Z. Y. Liu, K. F. Wang, J. Zhai, Organic/inorganic hybrid nanochannels based on polypyrrole-embedded alumina nanopore arrays: pH- and light-modulated ion transport. *Adv. Funct. Mater.* **25**, 2091–2098 (2015).
37. Y. He, D. Gillespie, D. Boda, I. Vlassiouk, R. S. Eisenberg, Z. S. Siwy, Tuning transport properties of nanofluidic devices with local charge inversion. *J. Am. Chem. Soc.* **131**, 5194–5202 (2009).
38. K. Y. Han, L. P. Heng, L. P. Wen, L. Jiang, Biomimetic heterogeneous multiple ion channels: A honeycomb structure composite film generated by breath figures. *Nanoscale* **8**, 12318–12323 (2016).
39. Z. Zhang, X. Y. Kong, K. Xiao, Q. Liu, G. H. Xie, P. Li, J. Ma, Y. Tian, L. P. Wen, L. Jiang, Engineered asymmetric heterogeneous membrane: A concentration-gradient-driven energy harvesting device. *J. Am. Chem. Soc.* **137**, 14765–14772 (2015).
40. C. C. Yu, X. B. Zhu, C. Y. Wang, Y. H. Zhou, X. T. Jia, L. Jiang, X. Liu, G. G. Wallace, A smart cyto-compatible asymmetric polypyrrole membrane for salinity power generation. *Nano Energy* **53**, 475–482 (2018).
41. X. B. Zhu, J. D. Zhong, J. R. Hao, Y. Z. Wang, J. J. Zhou, J. W. Liao, Y. J. Dong, J. H. Pang, H. B. Zhang, Z. Z. Wang, W. Zhang, W. T. Zheng, Z. H. Jiang, Y. H. Zhou, L. Jiang, Polymeric nano-blue-energy generator based on anion-selective ionomers with 3D pores and pH-driving gating. *Adv. Energy Mater.* **10**, 2001552 (2020).
42. W. P. Chen, Q. Wang, J. J. Chen, Q. R. Zhang, X. L. Zhao, Y. C. Qian, C. C. Zhu, L. S. Yang, Y. Y. Zhao, X. Y. Kong, B. Z. Lu, L. Jiang, L. P. Wen, Improved ion transport and high energy conversion through hydrogel membrane with 3D interconnected nanopores. *Nano Lett.* **20**, 5705–5713 (2020).
43. J. J. Chen, W. W. Xin, X. Y. Kong, Y. C. Qian, X. L. Zhao, W. P. Chen, Y. Sun, Y. D. Wu, L. Jian, L. P. Wen, Ultrathin and robust silk fibroin membrane for high-performance osmotic energy conversion. *ACS Energy Lett.* **5**, 742–748 (2020).
44. W. Xin, H. Xiao, X. Y. Kong, J. Chen, L. Yang, B. Niu, Y. Qian, Y. Teng, L. Jiang, L. Wen, Biomimetic nacre-like silk-crosslinked membranes for osmotic energy harvesting. *ACS Nano* **14**, 9701–9710 (2020).
45. H. C. Zhang, J. Hou, Y. X. Hu, P. Y. Wang, R. W. Ou, L. Jiang, J. Z. Liu, B. D. Freeman, A. J. Hill, H. T. Wang, Ultrafast selective transport of alkali metal ions in metal organic frameworks with subnanometer pores. *Sci. Adv.* **4**, eaaq0066 (2018).
46. A. Bhatnagar, E. Kumar, M. Sillanpaa, Nitrate removal from water by nano-alumina: Characterization and sorption studies. *Chem. Eng. J.* **163**, 317–323 (2010).
47. E. T. Acar, S. F. Buchsbaum, C. Combs, F. Fornasiero, Z. S. Siwy, Biomimetic potassium-selective nanopores. *Sci. Adv.* **5**, eaav2568 (2019).

Acknowledgments

Funding: This work was supported by the Ministry of Science and Technology (MOST), Taiwan, under the Shackleton Program award number 108-2638-E-002-003-MY2, and the other MOST grants (108-2221-E-011-103-MY3 and 108-2628-E-011-006-MY3). **Author contributions:** L.-H.Y. and K.C.-W.W. conceived and guided the project. Y.-C.L., L.-H.Y., and K.C.-W.W. designed the experiments. Y.-C.L. performed the experiments and conducted related characterization. M.-J.Z. helped sample preparation and SEM analyses. All authors contributed to analyze and discuss the results. Y.-C.L., L.-H.Y., and K.C.-W.W. cowrote the manuscript. **Competing interests:** The authors declare that they have no competing interests. **Data and materials availability:** All data needed to evaluate the conclusions in the paper are present in the paper and/or the Supplementary Materials.

Submitted 27 September 2020
Accepted 21 January 2021
Published 3 March 2021
10.1126/sciadv.abe9924

Citation: Y.-C. Liu, L.-H. Yeh, M.-J. Zheng, K. C.-W. Wu, Highly selective and high-performance osmotic power generators in subnanochannel membranes enabled by metal-organic frameworks. *Sci. Adv.* **7**, eabe9924 (2021).